A Robotic Platform to Navigate MRI-guided Focused Ultrasound System

Jing Dai[1], Zhuoliang He[1], Ge Fang[1], Xiaomei Wang[1], Yingqi Li[1], Chim-Lee Cheung[1], Liyuan Liang[2], Iulian Iordachita[3], *Senior Member, IEEE*, Hing-Chiu Chang[2], Ka-Wai Kwok[1], *Senior Member, IEEE*

***Abstract*— Focused ultrasound (FUS) technology attracts increasing interests accrediting to its non-invasive and painless treatment of tumors. Magnetic resonance imaging (MRI) guidance has been introduced to monitor this procedure, thus allowing the ultrasound foci to be precisely controlled. However, manual positioning of the FUS transducers is challenging, especially for the intra-operative (intra-op) adjustment in the MRI room. Currently, there are very few devices capable to provide robotic transducer positioning for the treatment of abdominopelvic organ diseases under MRI. The high intensity focused ultrasound (HIFU) spot would have to be "steered" to ablate large (>Ø 3.5 cm) or multiple tumors (e.g. in liver). To this end, we proposed a hydraulic-driven tele-operated robot platform that enables 5-DoF manipulation of the FUS transducer. Even operated close to the MRI iso-center, the robot can guarantee zero electromagnetic (EM) artifact to the MR image. Our proof-of-concept robot prototype can offer a large workspace (100mm×100mm×35mm) for FUS foci steering. Accurate manipulation (0.2 mm in translation, 0.4° in rotation) of the FUS transducer holder is achieved using rolling diaphragm-sealed hydraulic actuators. The robot control responsiveness (from 0.1 to 4 Hz) is also evaluated to show the potential to compensate for the spot tracking error induced by respiratory motion. We also demonstrate the use of wireless radiofrequency (RF) markers to continuously register the robot task space in the MRI coordinates.**

***Index Terms*— MRI-compatible robot, MRI-guided focused ultrasound, surgical robot navigation.**

I. Introduction

FUS is a non-invasive therapeutic technology that can focus ultrasound at specific target spots to induce micro-mechanical effects deep inside the body [3]. HIFU, as a typical FUS modality, has been established as an effective and safe incisionless alternative in the treatment of particular tumors, such as in prostate [4], uterus and liver accredit to its completely non-invasive and extracorporeal advantage. Current FUS has made remarkable progress in a few clinical conditions (e.g. uterine fibroids, bone pain palliation) although abdominal HIFU is in its early stage. For example, more than 10,000 patients with uterine fibroids have been treated with HIFU throughout the world since 2004 [5].

Manuscript received: October 15, 2020; Revised: March 16, 2021; Accepted: March 16, 2021. This paper was recommended for publication by Editor Pietro Valdastri upon evaluation of the Associate Editor and Reviewers comments. This work was supported in part by the Research Grants Council of Hong Kong under Grants 17207020, 17206818 and 17205919 and in part by the Innovation and Technology Commission of Hong Kong under Grants UIM/353 and ITS/403/18 and in part by the Multi-Scale Medical Robotics Center Limited, InnoHK under Grant EW01500.

[1]J. Dai, Z. He, G. Fang, X. Wang, Y. Li, C. L. Cheung and K. W. Kwok are with Department of Mechanical Engineering, The University of Hong Kong, Hong Kong, China (corresponding author, e-mail: kwokkw@hku.hk).

[2]L. Liang and H. C. Chang are with Department of Diagnostic Radiology, The University of Hong Kong, Hong Kong, China.

[3]I. Iordachita is with the Laboratory for Computational Sensing and Robotics, The Johns Hopkins University, USA.

Digital Object Identifier (DOI): see top of this page.

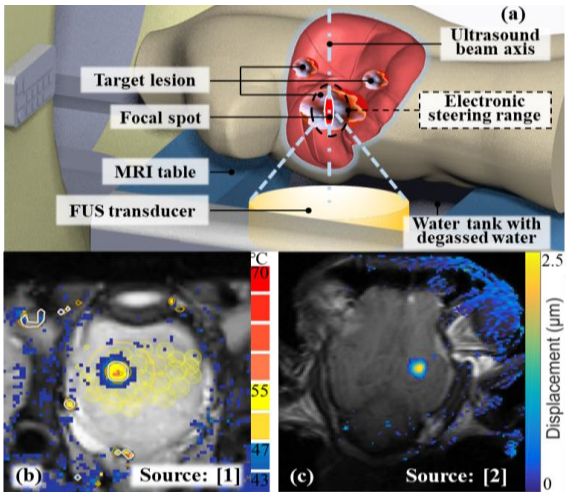

Fig. 1. (a) Schematics of MRI-guided FUS (MRg-FUS) therapy for liver tumors, where tissues on the FUS focal spot could be ablated. Patient lies in prone position with FUS transducer placed inside the water tank in the MRI table; **(b)** MR thermal imaging (in °C) during FUS treatment on uterine leiomyomas (Image source: [1]); **(c)** MR-ARFI of brain, revealing FUS-induced tissue displacement in micro scale (μm) (Image source: [2]).

Advanced FUS systems usually feature phased-array transducers, where the phase of each transducer in the aperture array could be independently adjusted. Such phased-array transduction enables dexterous electronic control of the acoustic beam direction and geometry, resulting in fast acoustic pattern shifting to accommodate small-range physiological motion [6]. However, such focal-spot adjustment range (e.g. Ø<4 cm [7]) along a given direction in the focal plane is still insufficient for abdominopelvic-organ treatment **(Fig. 1a).** The region of interest (RoI) there covering multiple lesion targets would be much larger than the focal region of a *fixed* transducer array, particularly when the targets (e.g. tumors in liver) are located deep inside and also moved by respiration. This requires additional mechanical displacement of the transducer to greatly enlarge the workspace. The common practice is to manually offset the transducer, but it would be time-consuming while involving re-positioning of patient and re-calibration for HIFU target tracking. Therefore, automatic adjustment is in demand to steer the foci covering the entire RoI.

It has been expected that the robotic navigation based on intra-op images can facilitate tele-manipulation of the transducers, thus greatly reducing the procedural time. HIFU lesion tracking to compensate physiological motion in a large range (e.g. >2 cm [8]) would also be realized. MRI [9] has been widely adopted in FUS treatments to provide intra-op guidance, attributing to its superior soft-tissue imaging contrast. Magnetic

resonance (MR) thermometry enables measurement of fine changes in tissue temperatures **(Fig. 1b)**, thus providing in-situ monitoring of HIFU ablation process. During MRg-FUS therapy, MR acoustic radiation force imaging (MR-ARFI) could be used for ultrasound focus spot visualization **(Fig. 1c)**. It has stimulated much research on developing robot-assisted MRg-FUS systems, where those for abdominal (e.g. liver) and pelvic organs (e.g. uterus, prostate) have been extensively investigated. Xiao *et al.* [10] employed a long robotic arm to increase the treatment region (500 mm translation and 40° rotation) for biopsy and FUS, but the arm had to be fixed outside the MRI bore. The table-mounted design would simply enlarge the manipulation range, but could not be transferred to practical abdominal FUS treatment. Note that for high-resolution imaging, an MR body coil has to be put on the abdomen/body, sparing very tight space for robot placement, thus making downward-facing FUS setting impossible.

The solution of coordinating FUS accessing and intra-op MRI guidance for abdominopelvic organs therapy was to place the robot underneath the prone-position patient [11] **(Fig. 1a)**. Subject to the confined space of sealed water tank (e.g. around 275mm×275mm [12, 13]) containing robot, the robot has to be compact in size, and also capable to offer large-range manipulation of transducers. Very few of the table-embedded robotic systems are commercially available especially for abdominal FUS. Sonalleve MRg-FUS system (Philips) and ExAblate 2000 (Insightec) are commercial MRg-FUS robotic systems, which are primarily developed for pelvic organ HIFU treatments. Unlike the stationary targets in pelvic FUS, it will be challenging for abdominal FUS, where fast focal spot tracking (> 0.2Hz [14]) is a mandatory prerequisite due to the rapid respiratory-induced motion. Platforms from MEDSONIC LTD (Cyprus) are featured with two translational DoFs, and predominantly produced for abdominal HIFU. However, such a 2-axis design could only allow motion in the coronal plane, which may restrict its capability of motion.

Although capable of accurate positioning within a sufficient steering range, most of the existing table-embedded systems are typically only applicable for low intensity FUS (e.g. hyperthermia). As can be seen in **Fig. 1c**, FUS energy could be absorbed by superficial regions; therefore, while taking account of skin burn [15] circumvents, the HIFU sonication would have to be paused frequently to ensure adequate "cool down" on the heated skin area [16]. LP-100 (FUS Instruments) and a lab-based platform designed by Yiannakou *et al.* [12] are motorized positioning systems for abdominal therapy with only translational DoFs. It was hypothesized by Yonetsuji *et al.* [16] that a robotic platform should flexibly rotate the transducer in a certain large angular range so as to reduce heat accumulation while fixing the focal spot. Therefore, their design without rotation may hamper the efficacy and cause skin burn.

To ensure a safe actuation for FUS robotic systems under (intra-op) MR environment while minimizing the interferences, various MR-conditional/MR-safe actuators were adopted, such as piezoelectric and ultrasonic actuators in gynecological tumors treatments [17]. However, the high-frequency current exciting the motor stepping action may induce significant artifacts on intra-op imaging [18], as the robot placed underneath the patient's abdomen would be very close (< 150 mm) to the isocenter of MRI scanner. Inherently MR safe motors powered by fluid, e.g. pneumatic motors [19, 20], have also been discussed. InnoMotion (InnoMedic GmbH) is a commercially available platform for biopsies and facet joint treatments, fully driven by pneumatic stepper motors. However, the high compressibility of air may cause mechanical transmission delay and thus control inaccuracies. The hydraulic system is accomplished with incompressible fluid as transmission media, offering quick response, accurate control and high-power density [21]. It was reported to navigate MRg-FUS with conventional piston-cylinder actuation from the 1990s [22]. But they only achieved a 3-DoF manipulation, causing an insufficient steering range with the absence of pan-and-tilt movement. To this end, we propose a tele-operated robot platform for MRg-FUS treatment in abdominopelvic organs [23]. The custom-made hydraulic robot actuation [21, 24] can ensure low transmission latency (100 ms on average under 4.5Hz) and high tracking accuracy (0.2 mm in translation, 0.4° in rotation), and MR-safety upon ASTM F2503. The robot setting allows the patient in prone position. Its sufficient DoFs enable the focal spot adjustable in a big volume inside the patient body. Our key work contributions are listed below:

1) Hydraulic actuation design of a 5-DoFs robot platform to navigate MRg-FUS system for abdominopelvic organ disease treatment, empowering the foci to be steered in a wide spatial coverage of major abdominal or pelvic organs.
2) Compact design of robot (240mm×180mm×190mm) capable to be accommodated in the water tank inside the MRI operating table for patient prone position.
3) Experimental evaluation of positional accuracy (max. error: 0.2 mm in translation, 0.4° in rotation), frequency response (0.1-4 Hz), MR-safety, and MR-based tracking features, thus demonstrating its potential for respiratory motion compensation.

II. Materials and Methods

This section presents the mechanism design and kinematics model of the proposed 5-DOF robotic manipulation. Here, the ultrasonic-transducer holder is considered as the robot end-effector. Such tele-manipulation can be simultaneously coordinated with the electronic control of sonication so as to target the lesions in abdominal or pelvic organ accurately, but decrease the risk of skin burn. The robotic system could be applied to some other abdominopelvic organs, such as the uterus, the prostate, and the kidney [25]. The biggest difference would be the patient's body posture, with the same goal to target the lesion area upon the acoustic window. Prone or supine posture will be determined based on the location of organ.

A. Robot Design Criteria

In our robot design and fabrication process, four major design criteria are taken in count as follows:

C1) **Workspace and dexterity**: Large manipulation range of HIFU beam has to be facilitated to cover a right lobe of adult liver with an average dimension of 140mm×140mm×140mm.

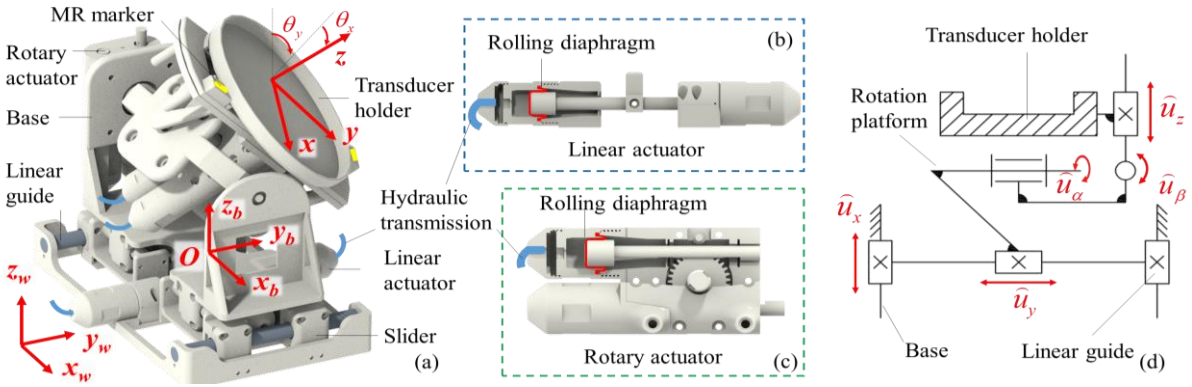

Fig. 2. (a) MRI-guided robotic manipulator for ultrasound transducer array positioning, with 3 translation DoFs and 2 rotation DoFs. The robot base and world coordinates are represented as $\{x_b, y_b, z_b\}$ and $\{x_w, y_w, z_w\}$, respectively, while the robot end-effector pose as $[x, y, z, \theta_x, \theta_y]$. Mechanism of the linear actuator **(b)** and rotary actuator **(c)** are illustrated; **(d)** Robot kinematics with their configuration variables.

To our simulation results, the horizontal translation is required with >15mm linear stroke in two perpendicular directions. Pan-tilt angular movement has to be >25°. Besides, those DoFs have to be operated independently to implement an irregular steering trajectory so as to "fill" the HIFU spot in a larger tumor (Ø > 5 cm) or "switch" the spot to multiple tumors.

C2) **Size and waterproof**: The robot should be compact to be housed inside the sealed water tank of a standard MRI-HIFU table, with a size of 275mm×275mm in L×W [12, 13]. Being immersed fully in water, the robot has to maintain dexterous manipulation against the water tension and resistance.

C3) **Targeting accuracy and responsiveness**: Minimum size (<Ø3 mm) of tumor would also be targeted. The robot has to steer the transducer holder in order to stabilize the HIFU foci at the target point with an error < 1 mm [26]. Meanwhile, to reduce the risk of skin burn and maintain an effective ablation, not only has the robot to make rapid response to alter the abdominal skin exposure to ultrasound, but it also has to compensate the respiration-induced motion, with an amplitude and frequency roughly of 9.95 ± 2.32 mm [27] and 0.2 Hz [14], respectively.

C4) **MR-Safety**: To the MR-safe standard of ASTM F2503 [28], the robot body has to be made of or fabricated with materials that are neither magnetic, metallic nor electrically conductive. Since the robot has to be coordinated simultaneously with the HIFU operation near to MRI iso-center, during the intra-op MR scanning, e.g. to view the thermometry or acoustic radiation force in the body, no EM interference or artifacts should be induced to adversely affect the imaging or even the tracking of our developed MR makers.

B. Robot Configuration and its Setup

To reduce the risk of skin-burn injury, two decoupled rotation DoFs, pan-tilt, are coordinated with the translation of transducers. Based on criteria C1), the follower robot is constructed with two translation platforms (namely lower and upper), integrated with a rotation platform in between, offering 5 DoFs of manipulation (**Fig. 2a**). Connected with the bottom framework of the robot through linear guides, the lower translation platform enables two perpendicular translation motions (35mm × 35mm) horizontally. For each DoF of the lower translation platform, there are four 3D-printed sliders holding the linear guide with two wheels up and down, thus eliminating the sliding friction to enable a smooth movement of the platform. The robot base (**Fig. 2a**) was built on top of the lower translation platform, housing the rotation platform with bearings. This guarantees the rotations in a range of ± 25° along two axes parallel to the lower platform translation. The upper translation platform was built on top of the rotation platform, follows the rotation along the y_b axis of the robot base. The purpose is to guide the normal force/translation relative to the rotation platform within the range of 35 mm. The transducer holder was built on top of it, following the upper translation platform movement. **Fig. 2d** illustrates our robot kinematics in a schematic diagram. Based on criteria C4), to minimize the interference during MR imaging process, the key components, such as the base and actuators were prototyped by 3D-printed polymer composites (VeroWhitePlus and MED610, Stratasys). The remaining parts such as the quick-fit connector on pipelines are also made of non-metallic and non-ferromagnetic materials. To register and track the robot end-effector into the MRI domain, our previously developed wireless RF-markers [29] are employed, which can be embedded in the transducer holder, giving rise to its 6-D continuous tracking with respect to (w.r.t.) the MR image coordinates (**Fig. 2a**).

C. Diaphragm-based Hydraulic Actuation

To provide quick response and low transmission latency, large output force, accurate control with MR-safe standard, In criteria C3), the diaphragm-based hydraulic actuation system is proposed. Each DoF is driven and transmitted through a pair of hydraulic pipelines. Our previous work [30], [31] reported the use of two-cylinder actuators that can generate rotary motions in a range of ± 90° **(Fig.2c)**. However, the central gear introduced for bidirectional motion did increase each unit in size to 120mm×58mm×28mm. Based on criteria C2), the robot should be compact in the confined space of the water tank, while enabling fully tele-manipulation inside the MRI operating table, we redesign the linear actuator (150mm×28mm×28mm) without central gear, but still capable to offer bidirectional linear motion with 35-mm stroke. The mirrored arrangement of two-cylinder units can reduce the dimension in weight direction as compared to the rotary actuator **(Fig.2c)**, despite its length increased instead **(Fig.2b)**. For applications involving linear movements only, such as the lower translation platform, this proposed linear actuator can be adopted to reduce the overall

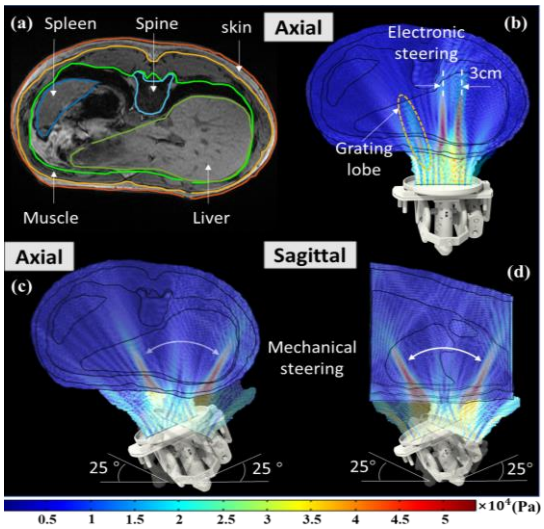

Fig. 3. (a) Segmented axial MR image for COMSOL simulation; **(b)** Proof-of-concept showing simulated acoustic interference with tissues and the limited electronic steering range (< 30 mm); Enlarged coverage range of acoustic spot conducted by robotic steering in **(c)** axial and sagittal **(d)** planes.

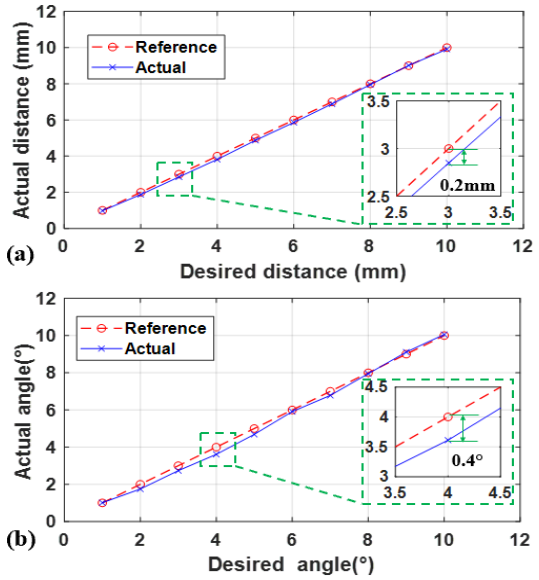

Fig. 4. Robot positioning accuracy test in one direction, with the translation **(a)** along *x*-axis and rotation **(b)** along *x*-axis.

robot footprint. To this end, two linear cylinders are integrated in the lower translation platform, and three rotary actuators are used in the remaining three DoFs, one for guiding the linear motion of transducer holder, the other two for its pan and tilt.

Rolling diaphragms (MCS2018M, FEFA Inc.) sealing a hydraulic pipeline at both ends are mainly made of fabric-reinforced rubber. Each diaphragm is capsulated in a cylinder, of which the stroke length is around 35 mm by the flipping inside-out motion of diaphragm, while rolling over the head of the piston rob under fluid pre-pressure of 0.1 Mpa [21]. A cylinder unit is connected with a metallic piston through a 10m pipeline filled with distilled water. Therefore, a bundle of pipelines has to be channeled via a waveguide in between the MRI and control room. Note that the connected piston (CDRQ2BS20-180, SMC) has to be actuated by electric motors in the control room. In our previous work [21], the actuation latency of the presented hydraulic transmission has been studied. It could be optimized by the selected pipeline material (semi-rigid nylon), and its inner diameter (Ø2 mm). Parts of rather elastic pipelines in spring shape are connected close to the cylinder ports, allowing certain flexibility, not to hinder the movement. However, these parts have to be short (<100mm) in length as which is a tradeoff with the actuation latency.

This hydraulic actuation design could enable the platform to be immersed and operated inside the tank of degassed water (criteria C2). In some cases, instead, degassed water can also be filled in a water bag (e.g. made of silicone) attached with a gel pad, separating the transducer and the patient.

D. Model-based Robot Control

Apart from the promising mechanical structure needed, analytical forward kinematics of the robot is required for model-based control. We take the robot status at rest as the initial status, and the center of the robot base as its coordinate origin, *O*. The task space is defined as the 5-D poses of the end-effector (i.e. the centroid of transducer holder) w.r.t. the coordinate shown in **Fig. 2a**. The pose of the end effector $\boldsymbol{p}=\left[x,y,z,\theta_x,\theta_y\right]^{\mathrm{T}}\in\mathbb{R}^5$ can be calculated as:

$$\boldsymbol{p}(\hat{\boldsymbol{u}})=\begin{bmatrix}(R+\hat{u}_z)\sin\hat{u}_\alpha+\hat{u}_x\\(R+\hat{u}_z)\sin u_\beta+\hat{u}_y\\l+(R+\hat{u}_z)\left(1-\sin^2\hat{u}_\alpha-\sin^2\hat{u}_\beta\right)^{1/2}\\\hat{u}_\alpha\\\hat{u}_\beta\end{bmatrix} \tag{1}$$

where $\hat{\boldsymbol{u}}=\left[\hat{u}_x,\hat{u}_y,\hat{u}_z,\hat{u}_\alpha,\hat{u}_\beta\right]^{\mathrm{T}}\in\mathbb{R}^5$ represents the robot configurations, which correspond to three translations along *x*, *y*, and *z* axes, as well as rotations along *x* and *y* axes; *l* is the depth of foci relative to end-effector. The transition mapping from configuration space to task space can be expressed as

$$\dot{\boldsymbol{p}}=\boldsymbol{J}\dot{\hat{\boldsymbol{u}}} \tag{2}$$

where the Jacobian matrix $\boldsymbol{J}$ can be calculated by differentiating the position $\boldsymbol{p}$ w.r.t. the input $\hat{\boldsymbol{u}}$. The inverse transition mapping can be established as:

$$\dot{\hat{\boldsymbol{u}}}=\boldsymbol{J}^{\dagger}\dot{\boldsymbol{p}} \tag{3}$$

where $\boldsymbol{J}^{\dagger}$ is the generalized inverse of $\boldsymbol{J}$. Notice that the configuration space parameters $\hat{\boldsymbol{u}}$ are defined on the robot part in the water tank, which are assumed linearly correlated with conductor-input. The correlation coefficients of translation and rotation motions are different, which are set as K_t and K_r respectively. That is,

$$\begin{aligned}\hat{u}_i&=K_t u_i,\ i=x,y,z.\\\hat{u}_j&=K_r u_j,\ j=\alpha,\beta.\end{aligned} \tag{4}$$

where $\boldsymbol{u}=\left[u_x,u_y,u_z,u_\alpha,u_\beta\right]^{\mathrm{T}}\in\mathbb{R}^5$ means the actuation command to conductor-side motors. To utilize the analytical model for actuation command calculation, registration from position tracking coordinate to the model coordinate (**Fig. 2a**) is required after the robot base is fixated inside the water tank.

E. Transducer Pose Tracking under MRI

Precise localization of transducer pose under MRI is the prerequisite to register the robot tasks in the MRI domain, where the HIFU planning takes place, hence enabling accurate targeting of ultrasound foci w.r.t to the treatment RoI. Our previous work proposed wireless MR-markers which enable

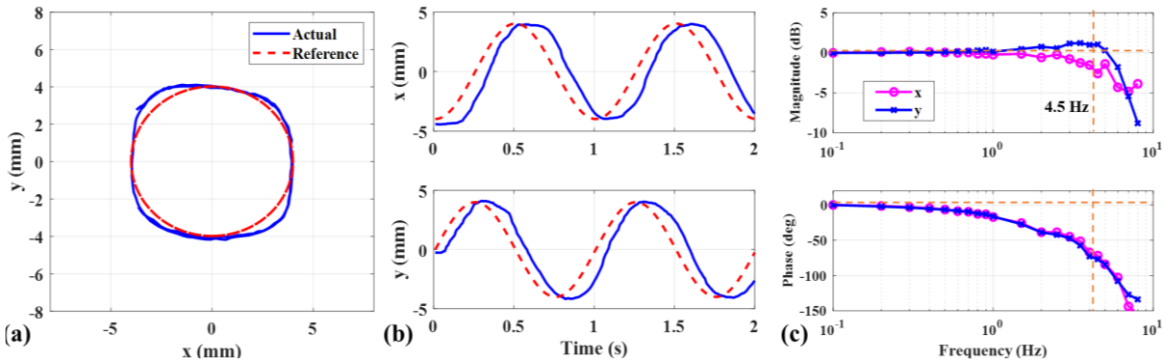

Fig. 5. Experimental results of frequency response. **(a)** Robot commanded to follow a circle in *x*-*y* (MRI coronal) plane at range of frequencies from 0.1 Hz to 4 Hz; **(b)** Sinusoidal response of the robot end-effector along *x* and *y* axis; **(c)** Bode plot of *x* and *y* translations sampled during the circular trajectory tracking.

continuous real-time positional tracking in MRI coordinates [29]. With a specific-designed circuit to amplify MR signal, the marker could provide high SNR compared to background even under low flip-angle (<1°) excitation. We integrated three markers on the transducer holder to detect its 6-D poses, including both the center position and normal direction of the end-effector. 1D-projection pulse-sequence can be applied so as to enable fast acquisition of positional signal (>30Hz). However, the signal profile of each marker may be influenced by the marker orientation and its distance to MR imaging coils. This would introduce signal noise into the detection of marker centroid, thus miss-calculating the end-effector pose. To ensure localization accuracy and maintain smooth tracking, we propose to use the robot kinematics model to predict the end-effector pose and combined with measured value from markers via Kalman filtering. The prediction model can be given as:

$$\begin{aligned} \hat{\boldsymbol{u}}_{t+\mathrm{d}t} &= \boldsymbol{K}\cdot \mathrm{d}\boldsymbol{u} + \hat{\boldsymbol{u}}_t + \boldsymbol{w}_t \\ \boldsymbol{p}_{t+\mathrm{d}t} &= \boldsymbol{J}\left(\hat{\boldsymbol{u}}_{t+\mathrm{d}t} - \hat{\boldsymbol{u}}_t\right) + \boldsymbol{p}_t + \boldsymbol{v}_t \end{aligned} \tag{5}$$

where $\boldsymbol{p}_{t+\mathrm{d}t}$ and $\boldsymbol{p}_t$ are the end-effector poses, $\hat{\boldsymbol{u}}_{t+\mathrm{d}t}$ and $\hat{\boldsymbol{u}}_t$ are the robot configurations, the subscript "$t+\mathrm{d}t$" and "t" denote the time step $t+\mathrm{d}t$ and t, $\boldsymbol{w}_t$ and $\boldsymbol{v}_t$ represent the process noise and observation noise. $\boldsymbol{K} = diag\left(\left[K_t, K_t, K_t, K_r, K_r\right]\right)$ is the mapping matrix co-relating actuation input from the control room to the robot output in the MRI room. The combined robot configuration can be computed as:

$$\hat{\boldsymbol{u}}^*_{t+\mathrm{d}t} = \hat{\boldsymbol{u}}_t + \boldsymbol{K}\cdot \mathrm{d}\boldsymbol{u} + \boldsymbol{G}\left(\boldsymbol{p}_{mea} - \boldsymbol{p}^*_t\right) \tag{6}$$

where $\boldsymbol{G}$ is the Kalman gain. Thus, the combined end-effector pose can be calculated using **Eq. (1)**, $\boldsymbol{p}^*_{t+\mathrm{d}t} = \boldsymbol{p}\left(\hat{\boldsymbol{u}}^*_{t+\mathrm{d}t}\right)$.

III. Results and Discussion

A. Simulation of Ultrasound Focusing

Acoustic simulation is performed as a preliminary study to guide our robot design, particularly in regard to the workspace requirement and the steering ranges of each robot DoF. Acoustic field was computed using finite element methods in Comsol Multiphysics (Comsol Inc). Liver is demonstrated as an example of the abdominopelvic organs that our robotic system targets, since the MRg-FUS treatment for liver would involve most of the challenging circumstances in that for abdominopelvic organs. The region of multiple tumors or a large tumor (>Ø 3.5 cm) in liver, the largest solid organ, inevitably requires a wider focal range compared to other solid organs. The electronic adjustment range (<3.5 cm) of focal spot may be insufficient to cover the target in liver. Another major difficulty comes from the dynamic tracking of a target under respiratory-induced liver motion [32]. Moreover, the acoustic energy would be dispersed quickly because of liver perfusion [33]. Higher acoustical power has to be therefore offered to overcome this loss. However, the increment of ultrasound power also increases the risk of skin burn and rib heating [33], due to more heat accumulation. As shown in **Fig. 3a,** a high-resolution axial MR image slice was acquired, its 3D geometry was created based on the manual segmented model. The block containing the liver is 140mm × 140mm × 140mm, excluding the left lobe which is adjacent to the air-filled lung so as cannot be accessed by ultrasound energy. A 9×9 phased-array transducer is 10 cm beneath the gel pal. Each transducer element has a diameter of 10 mm, then the transduction is initially planned by enabling all the simulated HIFU beams in phase at the target spot with 200-kHz frequency.

As a proof of concept, the acoustic field was computed to get the electronic steering range of the phased-array transducer. By tuning the phase, the simulated beam was kept steering till the ultrasound grating lobe appears [34] in the body media. Note that this grating lobe is unwanted, which may cause unnecessary tissue injury. **Fig. 3b** shows the beam displacement due to the electronic steering only. The acoustic beam is interfered with heterogeneous tissues/media simulated. The focal spot can be seen around the center of the liver right lobe. Transductions that allow the beam to move 10mm, 20mm, 30mm in horizontal direction are applied. The unwanted grating lobe appears when the beam moves 30mm. While fixing the transduction phases, the transducer holder was navigated by the

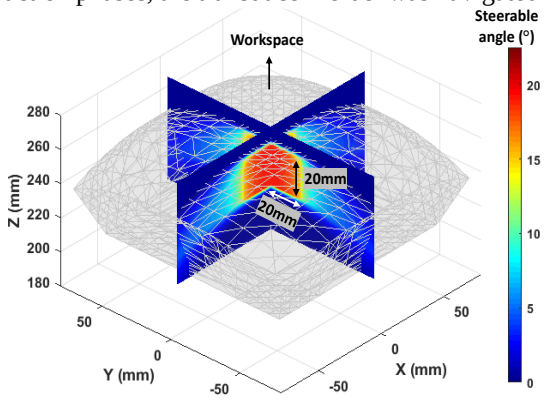

Fig. 6. Mechanical steering workspace of ultrasound foci. About each focal point, the robot enables a remote center of motion (RCM) to reduce accumulated exposure of a particular skin area. The larger steerable angular range of RCM, the warmer color at the focal point in the workspace.

robot, thus positioning the beam to cover the right lobe of liver. As shown in **Fig. 3c** and **3d**, relative to electronic steering, the mechanical motion of transducer can implement beamforming in a larger steering range. Such robot navigation just involves 15-mm translation and 25° rotation of the transducer holder.

B. Robot Positioning Accuracy

An experiment was conducted to validate the positioning accuracy along each DoF. As all translation DoFs are configured using the same linear actuation mechanism as in **Fig. 2b**, while two rotation DoFs are in **Fig. 2c**. The positional accuracy of translation and rotation are both illustrated in **Fig. 4**. A 6D EM tracker (Aurora, NDI Medical) was vertically attached on the edge of upper translation platform that carries the transducers. This EM-tracked pose acts as the positional ground truth. In the translation accuracy evaluation, 10 positions along the *x*-axis were defined with a 1-mm spacing (**Fig. 4a**). Based on the relationship between the motor's output angle and follower-side translation (**Eq. 4**), actuation command could be calculated. The robot was steered to attain all targets successively. The mean positioning error (involving 10 times repetition) of *x* translation DoF was 0.098 mm, and the maximum error was 0.2 mm. The mean rotation error was found to be 0.140°, with a maximum value of 0.4° (**Fig. 4b**). This positioning accuracy outperforms existing robotic platforms designed for the MRg-FUS system, among which a representative one could satisfy 0.2 mm translational (for 10 mm step) accuracy [11, 35].

C. Positional Frequency Response

A frequency response test was conducted to evaluate the dynamic performance of the robot. Our primary concern is on translational DoFs of robot base, which are most challenging for responsiveness due to the higher payload compared with other DoFs. The actuators of x and y DoFs were set to follow sinusoidal inputs with $\pi/2$ phase difference (**Fig. 5b)**, thus cooperatively tracing a circular trajectory (**Fig. 5a)**. Hydraulic transmissions from stepper motor input to robot output are realized using 10-m pipelines to meet the requirements of transmission length between the control room and scanner room.

The radius of the reference circle was set as 4mm, with the tracking frequency increased from 0.1 Hz to 8 Hz at an interval of 0.1Hz. The end-effector output motion was measured by a 6D EM tracking coil. In **Fig. 5c.** the bandwidth of *x* and *y* DoFs reaches about 4.5 Hz, at which the magnitude decreases -3 dB. The phase lag is kept less than 75° within the bandwidth. The transmission latency measured from the computer signal to robot output is 100 ms on average with the frequency < 4.5 Hz. The results demonstrate promising capability in compensating respiratory motion of liver with a frequency < 0.2Hz.

D. End-effector Pose Adjustment towards Fixed Focal Spot

To reduce the risk of skin burn while conducting ablation at a fixed target in tissue, the robot end-effector should be capable of providing remote center of motion (RCM) about the foci. With such RCM during ablation, the average exposure time of a particular skin region to ultrasound energy can be reduced, thus alleviating the heat accumulation.

As shown in **Fig. 6**, the reachable workspace of the focal point was calculated based on the robotic forward kinematics. The size of the workspace is about 100mm×100mm×35mm in L×W×H, which can be further enlarged by 40mm when combined with electronic steering. Here our focus is on the mechanical manipulation of focal point using robot. Around each foci, a maximum steerable angle of RCM was calculated to quantify the skin-burn prevention capability, which is varied with the focal point location. Therefore, it has been investigated that our robot with pan-tilt rotation DoFs is capable of decreasing heat accumulation on the skin. The steerable angle around the foci in two orthogonal slices is visualized by the warm color gradient. A maximum steerable angle of 20° can be provided for the focal point in the workspace center.

E. MR Compatibility Test

MR compatibility test (**Fig. 7a)** was conducted to evaluate the EM interference of the proposed robotic system to MR images using a 1.5T MRI scanner (SIGNA, General Electric Company, USA). The robot was tele-operated close to the MRI isocenter, so that we could conduct a more rigorous measurement of signal-to-noise (SNR) loss due to any EM image artifact, even not caused by the hydraulic actuation, but possibly by RF markers on the robot. An MRI water phantom (J8931, J.M. Specialty Parts, USA) was used to provide signal source, with a body coil attached for imaging. Both T1-weighted and T2-weighted images were acquired using fast field echo (FFE) and turbo spin-echo (TSE) sequences, respectively. Before introducing the robot to the scanner room, 3D MR images of the phantom were obtained as the baseline for SNR comparison. 3D imaging of the phantom was also performed while placing the robot beside the phantom. There are no observable image artifacts found in the MR images with the SNR loss < 2% (**Fig. 7b**), even when the robot is in operation. This offers the capability of performing MR imaging and robot actuation simultaneously, which is required for respiratory motion compensation and reducing the risk of skin burn. Supplementary video 1 shows the robot manipulation in the scanner recorded by MRI compatible camera.

F. MR-Based Tracking Test

Wireless MR markers were utilized to localize the robot end-effector in MR image coordinates. The markers are made of cylindrical glass tubes (Ø3 × 8mm) with Gadolinium-doped water (concentration: 10mM) sealed inside to provide signal source. Miniaturized RF-coil (1.5mm×6.7mm[29]) was attached on the tubes to locally amplify MR signal, thus offering high image contrast against background. $CuSO_4$ solution was introduced in the hydraulic actuation to decrease the T1 relaxation time of water, thus eliminating the background signal from actuation liquid. As shown in **Fig. 8a**, with the positions of three markers obtained, we can register the robot initial pose to the MR image coordinates. 1D projection pulse sequence is employed to enable real-time tracking of marker positions. **Fig. 8b** shows the intensity profile of 1D projection signal, where the peaks of markers can be extracted along the projected axis. 3D positions of markers can be

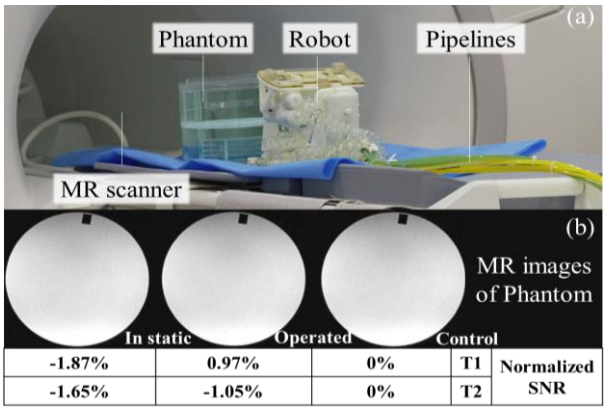

-1.87%	0.97%	0%	T1	Normalized SNR
-1.65%	-1.05%	0%	T2	

Fig. 7. (a) Robot and phantom placed close to the isocenter of the 1.5T MRI scanner; **(b)** Negligible EM interference found from the MR images of an MRI phantom put aside the robot. The normalized SNR results of T1 and T2 under three operation conditions are summarized in the table.

accordingly solved by imposing geometry constraints, e.g. the relative position of markers, on the possible combination of 1D marker coordinate. A real-time tracking test was conducted by continuously performing 1D projection scan with the markers moved by the robot. **Fig. 8c** gives the time-series projection image along *x*-axis in a period of 40s, with a temporal resolution of 12ms. The marker image demonstrates high contrast against the background, which can be automatically detected to provide real-time positional feedback under MRI.

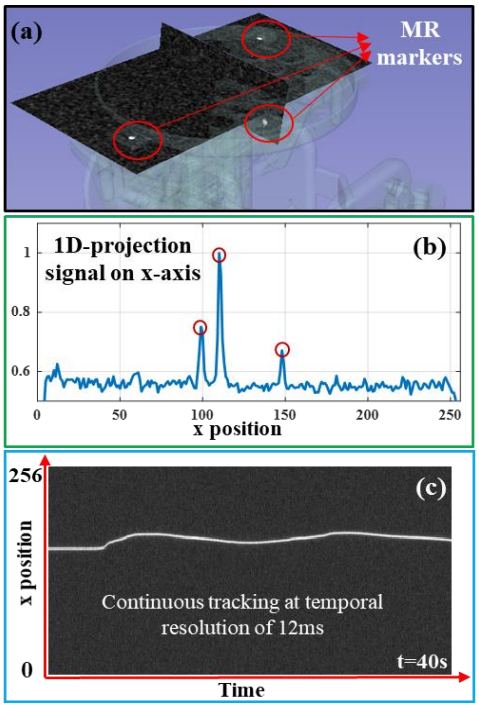

Fig. 8. (a) Three MR marker positions obtained from MR image to register robot in MRI coordinates; **(b)** 1D projection signal of three markers along *x* axis; **(c)** Continuously projected position on *x*-axis acquired at 83.3Hz. The SNR is so high that a single point signal within 0-256 pixel can be contrasted and observed at each time step.

IV. Conclusions and Future Work

In this letter, we present our proof-of-concept of a 5-DoF tele-manipulated positioning system for MRg-FUS treatment in abdominopelvic organs. It is a compact robot that can incorporate 3-DoF translation and 2-DoF rotation of FUS transducer array, which would be the first of its kinds facilitating the largest acoustic window to track HIFU spot inside patient body, as well as the most degree of flexibility to avoid residual sonication-induced skin burn. The performance of RCM demonstrates its capability to reduce the risk of skin-burn in clinical treatments. However, the steerable angle of RCM decreased fast when the focal point is away from the workspace center, where the hydraulic actuators would reach maximum stroke. One solution is to improve the hydraulic actuators with larger motion stroke, e.g. continuous motor equipped with 3 cylinders providing unlimited rotation range [21]. Accrediting to hydraulic actuation with fast-response (4.5-Hz bandwidth, 100-ms delay), this robot has the potential to compensate physiological motion, thus enabling to track a moving lesion target to provide safe and clinically effective treatment. The positional frequency response has been validated on the two DoFs moving the robot base along the MRI coronal plane. The sufficiency to perform respiratory motion (<0.2 Hz) compensation proves that our system could meet the HIFU speed requirements. By replacing the stepper motors, the high-end velocity servoing motors could be incorporated with the aim to further improve the tracking responsiveness and dynamics in whole in future designs. High positioning accuracy w.r.t. translation (max. error: 0.2 mm) and rotation (max. error: 0.4°) indicated that our system satisfies the typical accuracy requirements in clinical HIFU [36]. It would offer fine mechanical steering, along with the electronic control of HIFU spot. Note that the foci locations are measured from the lesion centroids on MR images. The positioning accuracy test undertaken in this study is only indicative of the transducer holder positioning itself, without considering some factors in clinical scenarios (e.g. tractive and shear forces induced from movements of the transducer in water, inherent MRI image distortion, and resolution limitations). Our proposed system is equipped with wireless RF markers, which enables continuously register the robot task space in the MRI coordinates. The positioning accuracy could be further improved by incorporating MR safe encoders (e.g. ZapFREE® MR431, Micronor Inc.) to each DoF of the robot. Furthermore, robust feedback control can be implemented by fused sensory information from the encoders and MRI feedbacks. The large-volume workspace (100mm×100mm×35mm) is evaluated by simulation, indicating the possibility to handle big-tumor or multi-tumor treatment in large abdominopelvic organs (e.g., adult liver, ~16 mm length in right lobe). The compatibility with MRI and real-time MR-based tracking have also been verified, respectively, by SNR test and 1D-projection technique. Our robot actuation is proved to induce no observable artifacts using sensitive 1D-projection pulse-sequence, even when the robot is actuated near the scanner isocenter. The robotic system could be applicable to some abdominopelvic organs, but it is still limited in some special clinical cases. For example, the system may not be applicable when tumor is adjacent to the vessels of the organs due to the cooling effect of blood flow [33].

As a proof-of-concept study, we demonstrate its promising potential for abdominopelvic organ tumor treatment. In the future, more extensive testing in and preclinical *in-vivo/ex-vivo*

HIFU with the presented robot is required to improve the system's capability for MRg-FUS abdominopelvic treatment. For example, MR compatibility test needs to be further evaluated, because high-frequency electric current exciting the piezoelectric transducers and encoders would induce MR artifacts on intra-op imaging. In addition to HIFU in this letter, recent advances of FUS technology also facilitates other treatments, such as hyperthermia-mediated drug delivery. We will also investigate the transducer phase modulation (i.e., electronic steering), and its combination with robotic steering for the relevant FUS applications, such as particular acoustic pattern forming under intra-op MRI.

REFERENCES

[1] B. Keserci *et al.*, "Volumetric MRI-guided, high-intensity focused ultrasound ablation of uterine leiomyomas: ASEAN preliminary experience," *Diagnostic and Interventional Radiology*, vol. 26, no. 3, p. 207, 2020.

[2] P. Gaur *et al.*, "Histologic safety of transcranial focused ultrasound neuromodulation and magnetic resonance acoustic radiation force imaging in rhesus macaques and sheep," *Brain stimulation*, vol. 13, no. 3, pp. 804-814, 2020.

[3] Y.-H. Hsiao, S.-J. Kuo, H.-D. Tsai, M.-C. Chou, and G.-P. Yeh, "Clinical application of high-intensity focused ultrasound in cancer therapy," *Journal of cancer*, vol. 7, no. 3, p. 225, 2016.

[4] A. Napoli *et al.*, "Real-time magnetic resonance–guided high-intensity focused ultrasound focal therapy for localised prostate cancer: preliminary experience," *European urology*, vol. 63, no. 2, pp. 395-398, 2013.

[5] M. Bohlmann, F. Hoellen, P. Hunold, and M. David, "High-intensity focused ultrasound ablation of uterine fibroids–potential impact on fertility and pregnancy outcome," *Geburtshilfe und Frauenheilkunde*, vol. 74, no. 2, p. 139, 2014.

[6] H. Q. Lean and Y. Zhou, "Acoustic field of phased-array ultrasound transducer with the focus/foci shifting," *Journal of Medical Biological Engineering*, vol. 39, no. 6, pp. 919-931, 2019.

[7] W. Chang *et al.*, "A portable high-intensity focused ultrasound system for the pancreas with 3D electronic steering: a preclinical study in a swine model," *Ultrasonography*, vol. 37, no. 4, p. 298, 2018.

[8] C. Y. An, Y. L. Hsu, and C. S. Tseng, "An Ultrasound-Guided Robotic HIFU Ablation System with Respiration Induced Displacement and Time Delay Compensation," *Journal of Medical Biological Engineering*, vol. 39, no. 5, pp. 796-805, 2019.

[9] I. S. Elhelf, H. Albahar, U. Shah, A. Oto, E. Cressman, and M. Almekkawy, "High intensity focused ultrasound: the fundamentals, clinical applications and research trends," *Diagnostic Interventional Imaging*, vol. 99, no. 6, pp. 349-359, 2018.

[10] X. Xiao, Z. Huang, M. A. Rube, and A. Melzer, "Investigation of active tracking for robotic arm assisted magnetic resonance guided focused ultrasound ablation," *The International Journal of Medical Robotics Computer Assisted Surgery*, vol. 13, no. 3, p. e1768, 2017.

[11] C. Damianou, M. Giannakou, G. Menikou, and L. Ioannou, "Magnetic resonance imaging-guided focused ultrasound robotic system with the subject placed in the prone position," *Digital Medicine*, vol. 6, no. 1, p. 24, 2020.

[12] M. Yiannakou, G. Menikou, C. Yiallouras, C. Ioannides, and C. Damianou, "MRI guided focused ultrasound robotic system for animal experiments," *The International Journal of Medical Robotics Computer Assisted Surgery*, vol. 13, no. 4, p. e1804, 2017.

[13] T. Sainio *et al.*, "Wedged gel pad for bowel manipulation during MR-guided high-intensity focused ultrasound therapy to treat uterine fibroids: a case report," *Journal of therapeutic ultrasound*, vol. 6, no. 1, pp. 1-10, 2018.

[14] D. Melodelima, W. A. N'Djin, N. R. Miller, J. C. Bamber, and J.-Y. Chapelon, "Comparative study of the effects of respiratory motion on in-Vivo hIFU treatments in the liver," in *2009 IEEE International Ultrasonics Symposium*, 2009: IEEE, pp. 1314-1317.

[15] L. Zhang *et al.*, "High-intensity focused ultrasound (HIFU): effective and safe therapy for hepatocellular carcinoma adjacent to major hepatic veins," *European radiology*, vol. 19, no. 2, p. 437, 2009.

[16] T. Yonetsuji *et al.*, "A novel high intensity focused ultrasound robotic system for breast cancer treatment," in *International Conference on Medical Image Computing and Computer-Assisted Intervention*, 2013: Springer, pp. 388-395.

[17] E. Epaminonda, T. Drakos, C. Kalogirou, M. Theodoulou, C. Yiallouras, and C. Damianou, "MRI guided focused ultrasound robotic system for the treatment of gynaecological tumors," *The International Journal of Medical Robotics Computer Assisted Surgery*, vol. 12, no. 1, pp. 46-52, 2016.

[18] H. Su *et al.*, "A MRI-guided concentric tube continuum robot with piezoelectric actuation: a feasibility study," in *2012 IEEE International Conference on Robotics and Automation*, 2012: IEEE, pp. 1939-1945.

[19] H. Su, G. A. Cole, and G. S. Fischer, "High-field MRI-compatible needle placement robots for prostate interventions: pneumatic and piezoelectric approaches," *Advances in robotics and virtual reality*, pp. 3-32, 2012.

[20] S. Eslami, G. S. FISCHER, J. Tokuda, and I. I. Iordachita, "Clinically Optimal Design and Development of an MRI-compatible Surgical Manipulator for the Prostate Percutaneous Intervention," in *9th Interventional MRI Symposium (iMRI)*, Boston, MA, USA, Sept 2012.

[21] Z. Dong *et al.*, "High-performance continuous hydraulic motor for MR safe robotic teleoperation," *IEEE Robotics and Automation Letters*, vol. 4, no. 2, pp. 1964-1971, 2019.

[22] R. H. Ettinger, H. E. Cline, R. D. Watkins, and K. W. Rohling, "Magnetic resonance guided ultrasound therapy system with inclined track to move transducers in a small vertical space," ed: Google Patents, 1994.

[23] K. W. Kwok, Z. He, J. Dai, G. Fang, and X. Wang, "A Robotic Platform to Navigate MRI-guided Focused Ultrasound System," Provisional Patent. 63/159,392 Mar. 10, 2021.

[24] Z. He *et al.*, "Design of a percutaneous MRI-guided needle robot with soft fluid-driven actuator," *IEEE Robotics and Automation Letters*, vol. 5, no. 2, pp. 2100-2107, 2020.

[25] Y.-s. Kim, "Advances in MR image-guided high-intensity focused ultrasound therapy," *International Journal of Hyperthermia*, vol. 31, no. 3, pp. 225-232, 2015.

[26] A. Dupre et al., "Evaluation of the feasibility, safety, and accuracy of an intraoperative high-intensity focused ultrasound device for treating liver metastases," *Journal of Visualized Experiments*, no. 143, p. e57964, 2019.

[27] Y. Hu, Y. K. Zhou, Y. X. Chen, S. M. Shi, and Z. C. Zeng, "4D-CT scans reveal reduced magnitude of respiratory liver motion achieved by different abdominal compression plate positions in patients with intrahepatic tumors undergoing helical tomotherapy," *Medical physics*, vol. 43, no. 7, pp. 4335-4341, 2016.

[28] A. International, "ASTM F2503-13: Standard practice for marking medical devices and other items for safety in the magnetic resonance environment," ed, 2013.

[29] C.-L. Cheung, J. D.-L. Ho, V. Vardhanabhuti, H.-C. Chang, and K.-W. Kwok, "Design and Fabrication of Wireless Multilayer Tracking Marker for Intraoperative MRI-Guided Interventions," *IEEE/ASME Transactions on Mechatronics*, vol. 25, no. 2, pp. 1016-1025, 2020.

[30] K.-H. Lee *et al.*, "MR safe robotic manipulator for MRI-guided intracardiac catheterization," *IEEE/ASME Transactions on Mechatronics*, vol. 23, no. 2, pp. 586-595, 2018.

[31] Z. Guo *et al.*, "Compact design of a hydraulic driving robot for intraoperative MRI-guided bilateral stereotactic neurosurgery," *IEEE Robotics and Automation Letters*, vol. 3, no. 3, pp. 2515-2522, 2018.

[32] A. Diodato, A. Cafarelli, A. Schiappacasse, S. Tognarelli, G. Ciuti, and A. Menciassi, "Motion compensation with skin contact control for high intensity focused ultrasound surgery in moving organs," *Physics in Medicine & Biology*, vol. 63, no. 3, p. 035017, 2018.

[33] J. Wijlemans *et al.*, "Magnetic resonance-guided high-intensity focused ultrasound (MR-HIFU) ablation of liver tumours," *Cancer Imaging*, vol. 12, no. 2, p. 387, 2012.

[34] M. Wang and Y. Zhou, "High-intensity focused ultrasound (HIFU) ablation by frequency chirp excitation: reduction of the grating lobe in axial focus shifting," *Journal of Physics D: Applied Physics*, vol. 51, no. 28, p. 285402, 2018.

[35] C. Y. An, J. H. Syu, C. S. Tseng, and C.-J. Chang, "An ultrasound imaging-guided robotic HIFU ablation experimental system and accuracy evaluations," *Applied Bionics Biomechanics*, vol. 2017, 2017.

[36] T. Tang *et al.*, "A new method for absolute accuracy evaluation of a US-guided HIFU system with heterogeneous phantom," in *2016 IEEE International Ultrasonics Symposium (IUS)*, 2016: IEEE, pp. 1-4.